ACS APPLIED ENERGY MATERIALS

www.acsaem.org Article

$Li_4Ti_5O_{12}$ Nanoshell on TiO_2 Nanofibers as a Durable Anode for Li-Ion Battery Energy Storage

Ching-Kit Ho, Chi-Ying Vanessa Li,* Changzhong Liao,‖ Yee-Yan Tay,‖ Ka-Ming Leung,‖ Chi-Kin Jenkin Tsui, GuanHua Chen, and Kwong-Yu Chan*

Cite This: *ACS Appl. Energy Mater.* 2023, 6, 11433−11441 Read Online

ACCESS | Metrics & More | Article Recommendations | Supporting Information

ABSTRACT: TiO_2(B), despite its high theoretical capacity, suffers from a dramatic initial irreversible capacity loss (ICL), thus hindering its application as an anode material in lithium-ion batteries (LIBs). In this work, we successfully construct a $Li_4Ti_5O_{12}$ nanoshell on TiO_2 nanofibers, in which the pristine TiO_2 nanofibers are mixed phases of TiO_2(B) and anatase TiO_2. Benefiting from the effective protection of the TiO_2 surface by the $Li_4Ti_5O_{12}$ nanoshell and the presence of abundant $Li_4Ti_5O_{12}/TiO_2$ nanointerfaces, the resulting $Li_4Ti_5O_{12}$−TiO_2 nanofibers (LTO−TiO_2) demonstrate negligible ICL with enhanced rate capability and consistent performance over prolonged cycles. This work not only demonstrates that LTO−TiO_2 can be utilized as a viable LIB energy storage material with high energy density (380 W h kg^{-1}) but also gives an insight into the strategy of using $Li_4Ti_5O_{12}$ as a nanoshell to mitigate the SEI formation and eliminate the initial irreversible capacity loss of other electrodes.

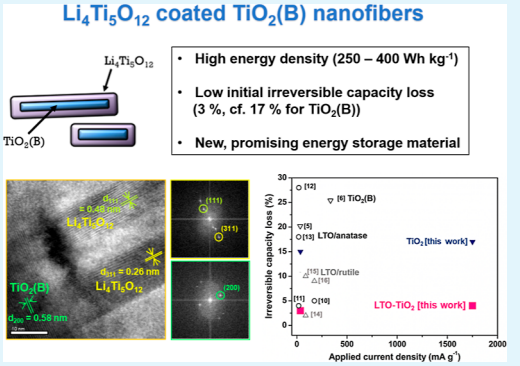

KEYWORDS: *lithium titanate, titania nanofibers, titania hybrid electrode, lithium-ion batteries, initial irreversible capacity loss, nanoshell, energy storage, SEI mitigation*

INTRODUCTION

TiO_2 polymorphs, including anatase, rutile, and TiO_2(B) (bronze), have been extensively studied for lithium-ion batteries (LIBs) as titanium anode alternatives to the commercialized $Li_4Ti_5O_{12}$ (LTO).[1] These TiO_2 polymorphs exhibit theoretical capacity [335 mA h g^{-1} for TiO_2(B); 168 mA h g^{-1} for anatase and rutile] and lithiation/delithiation potential (1.4−1.8 V vs Li^+/Li) comparable to that of LTO (175 mA h g^{-1}, 1.55 V vs Li^+/Li), which is sufficient to provide a high energy density without causing safety concern related to lithium dendrite formation. However, these TiO_2 polymorphs still have drawbacks. In general, TiO_2 suffers from the initial irreversible capacity loss (ICL), due to the facile solid−electrolyte interphase (SEI) formation by electrolyte reduction on the TiO_2 surface.[2,3] Such an electrically insulating SEI layer limits the high-rate performance of TiO_2. TiO_2(B) in particular can have significant ICL as high as 20−40%,[4−6] while for anatase and rutile TiO_2 is around 10%. In contrast, $Li_4Ti_5O_{12}$ (LTO) has high stability toward the electrolyte, resulting in minimal SEI formation and negligible initial ICL.[7] Although LTO has a lower theoretical capacity (175 mA h g^{-1}), it provides excellent cyclability and delivers a flat voltage plateau with negligible volume expansion (0.2%) during lithiation/delithiation (cf. 4% for TiO_2).[8]

One of the main applications of lithium-ion batteries (LIBs) is grid energy storage, which demands not only high energy density but also safe and stable cycling with little capacity depreciation over long-term operation. High power density (related to fast charge/discharge ratio) is a relatively less significant consideration for grid energy storage. Although graphite anode can offer higher theoretical energy density than typical TiO_2 and LTO anodes, its extremely low lithiation/delithiation potential can cause excessive lithium plating and uncontrollable growth of lithium dendrite during repeated cycling and in turn increase the risk of fatal internal short circuit and explosion. In comparison with graphite, TiO_2 and LTO anodes have much higher lithiation/delithiation potential with longer calendar life and cycle life and thus are more suitable candidates as LIB electrode materials for grid-energy storage application.

To address the demands for high-performance and stable TiO_2 and LTO anodes, there are increasing efforts to develop TiO_2-based multiphase nanostructures with low-energy barrier interfaces for charge transport.[9] Dual-phase $Li_4Ti_5O_{12}$/anatase TiO_2,[10−13] $Li_4Ti_5O_{12}$/rutile TiO_2,[14−16] TiO_2(B)/anatase TiO_2,[17−19] and anatase/rutile TiO_2 nanostructures[4] have been reported for enhanced performance. However, no

Received: May 19, 2023
Revised: October 25, 2023
Accepted: October 25, 2023
Published: November 13, 2023

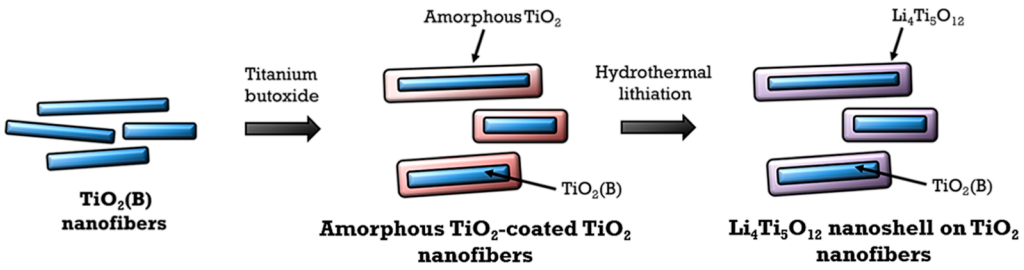

Figure 1. Synthesis and formation mechanism of the $Li_4Ti_5O_{12}$ nanoshell on TiO_2 nanofibers (LTO−TiO_2).

previous reports utilize the SEI-free property of LTO by coating it on TiO_2 to eliminate SEI formation. Either phase separation between LTO and TiO_2[10−13,16] or TiO_2 coating on LTO particles[14,15,20] are reported. In our previous study,[21] the TiO_2(B)/$Li_4Ti_5O_{12}$ nanofiber (denoted as TB/LTO) is synthesized via one-step hydrothermal lithiation of pristine TiO_2(B) nanofibers. As for TB/LTO, $Li_4Ti_5O_{12}$ (LTO) is only preferentially grown at the both ends of TiO_2(B) nanofibers, resulting in dumbbell-like morphology; due to the preferred lattice commensurability between the (020) plane of TiO_2(B) and $Li_4Ti_5O_{12}$.[21] To further reduce the SEI formation of TiO_2, it would be desirable to cover the pristine TiO_2 fibers fully with $Li_4Ti_5O_{12}$. Herein, for the first time, we develop a new strategy to construct a $Li_4Ti_5O_{12}$ nanoshell that fully covers TiO_2 nanofibers. This will mitigate SEI formation and thereby increase its stability and long-term capacity of TiO_2. The LTO nanoshell structure, the core TiO_2 nanofiber, and the interface between them are analyzed, and electrochemical contributions of each region are discussed.

RESULTS AND DISCUSSION

$Li_4Ti_5O_{12}$ nanoshell on TiO_2 nanofibers (LTO−TiO_2) is fabricated via a two-step postsynthesis of TiO_2 nanofibers (TiO_2) consisting of mainly TiO_2(B). As illustrated in Figure 1, it first involves synthesizing an amorphous TiO_2 (a-TiO_2) layer entirely around TiO_2 nanofibers, followed by hydrothermal lithiation of the a-TiO_2 layer to form the $Li_4Ti_5O_{12}$ (LTO) nanoshell on TiO_2 nanofibers. Details of the synthesis can be found in the Experimental Section.

Successful integration of LTO into TiO_2 is evidenced by high-resolution XRD (HR-XRD) and microscopy results. With the LTO coverage on TiO_2 (i.e., LTO−TiO_2), the major XRD diffraction peaks of spinel $Li_4Ti_5O_{12}$ (JCPDS no. 49-0207) clearly appear along with the monoclinic TiO_2(B) peaks (JCPDS no. 46-1238) and anatase TiO_2 peaks (JCPDS no. 75-1537) as demonstrated in the Rietveld refinement (goodness-of-fit: 1.5), as shown in Figure 2a. The composition of LTO−TiO_2 derived from Figure 2a is determined to be 27.1 wt % $Li_4Ti_5O_{12}$, 38.4 wt % TiO_2(B), and 34.5 wt % anatase TiO_2 using quantitative Rietveld refinement method (Table 1). The lattice parameters and crystallite size with respect to TiO_2(B), LTO, and anatase TiO_2 are also calculated using the Scherrer equation, and summarized in Table 1. The LTO−TiO_2 composite shows only negligible change in lattice parameters (a, b, c) of TiO_2(B), suggesting $Li_4Ti_5O_{12}$ is formed outside the TiO_2 fibers without disturbing the entire lattice of TiO_2(B). However, there is still an increase in the crystallite size of TiO_2 from its pristine form to LTO−TiO_2, which can be attributed to the crystal growth of TiO_2 fibers during the hydrothermal lithiation under elevated temperature. The intermediate amorphous TiO_2-coated TiO_2 nanofibers (a-

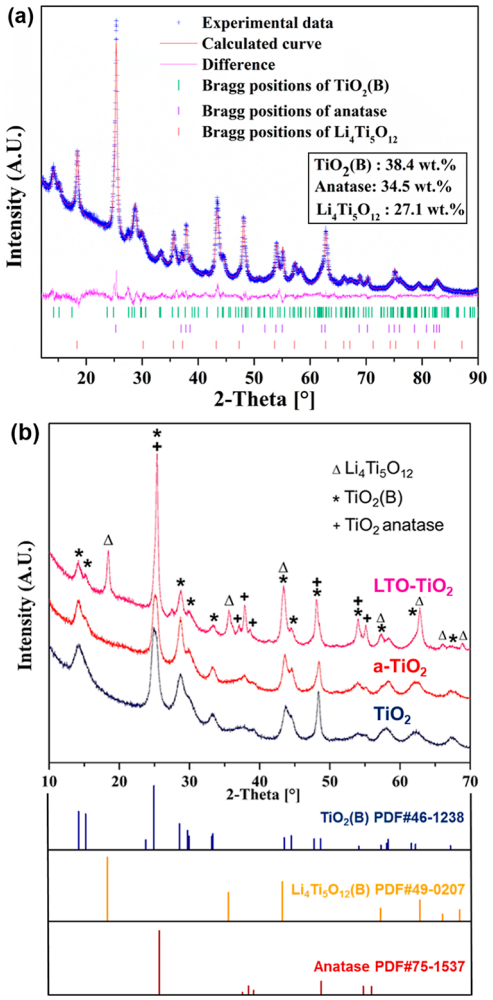

Figure 2. (a) HR-XRD patterns of $Li_4Ti_5O_{12}$ nanoshell on TiO_2 nanofibers (LTO−TiO_2) with Rietveld refinement (goodness-of-fit: 1.5), and the corresponding peak decomposition into $Li_4Ti_5O_{12}$, TiO_2(B), and anatase TiO_2. (b) HR-XRD patterns of $Li_4Ti_5O_{12}$ nanoshell on TiO_2 nanofibers (LTO−TiO_2), the intermediate phase of amorphous TiO_2-coated TiO_2 nanofibers (a-TiO_2), and pristine TiO_2 (TiO_2).

TiO_2) have similar XRD patterns of TiO_2(B) and anatase as that of pristine TiO_2 nanofibers (Figure 2b).

As shown by SEM images in Figure 3a,b, LTO−TiO_2 retains the nanofiber morphology of pristine TiO_2 (Figure S1), but with a larger fiber diameter of 200−350 nm (cf. 20−200 nm for pristine TiO_2) and a rugged surface due to the LTO nanoshell. From the HRTEM analysis in Figure 3c, LTO−TiO_2 nanofibers are uniformly covered by jagged-shaped nanocrystals with a thickness of 60 nm, forming a pseudocore/

https://doi.org/10.1021/acsaem.3c01213
ACS Appl. Energy Mater. 2023, 6, 11433−11441

Table 1. Summary of the wt % Composition, Lattice Parameter (Å), and Crystallite Size (nm) of the Samples Calculated Using Rietveld Refinement from HR-XRD

			$Li_4Ti_5O_{12}$ nanoshell on TiO_2 (LTO-TiO_2)	amorphous TiO_2 on TiO_2 (intermediate phase, a-TiO_2)	pristine TiO_2 (TiO_2)
composition (wt %)	TiO_2(B)		38.4	83.3	86.2
	$Li_4Ti_5O_{12}$		27.1	0	0
	anatase TiO_2		34.5	16.7	13.8
lattice parameter (Å)	TiO_2(B)	*a*	12.204	12.195	12.203
		b	3.757	3.760	3.763
		c	6.523	6.524	6.521
	$Li_4Ti_5O_{12}$	*a* = *b* = *c*	8.364	n/a	n/a
	anatase TiO_2	*a* = *b*	3.788	3.786	3.778
		c	9.509	9.518	9.497
crystallite size (nm)	TiO_2(B)		8.7	7.3	5.6
	$Li_4Ti_5O_{12}$		11.9	n/a	n/a
	anatase TiO_2		17.0	9.6	8.7

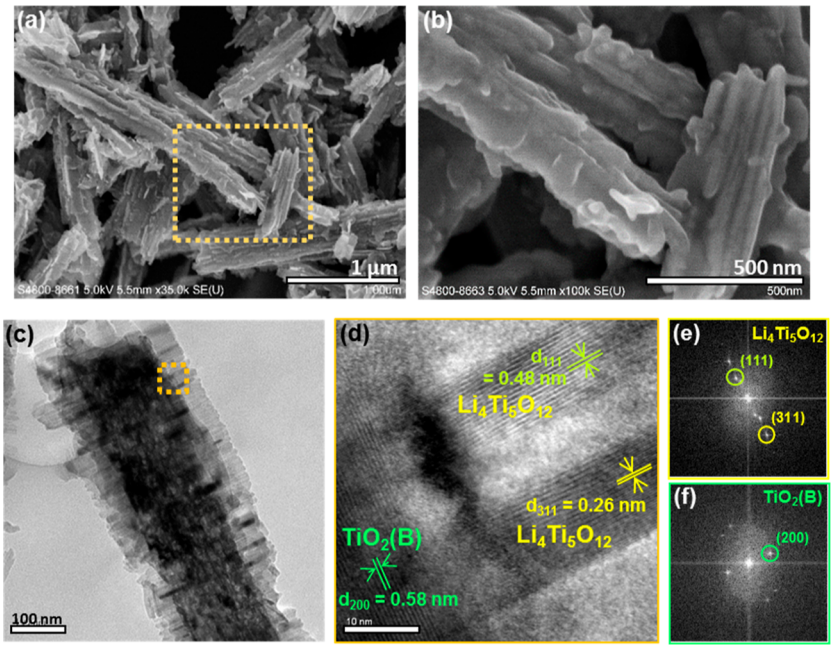

Figure 3. SEM images of (a) LTO−TiO_2 and (b) the respective enlarged region highlighted in yellow box in (a). (c) TEM image of LTO−TiO_2 showing the core of TiO_2 uniformly covered by $Li_4Ti_5O_{12}$ nanoshell, and (d) HRTEM image of the enlarged yellow square region in (c), showing the jagged-shaped nanocrystals on LTO−TiO_2 nanofibers, with the respective FFT images taken on the region of (e) $Li_4Ti_5O_{12}$ nanocrystals and (f) TiO_2 nanofibers from figure (d).

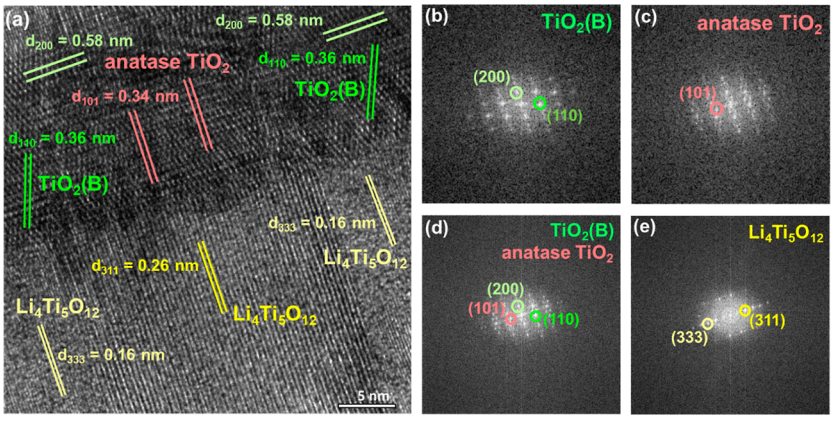

Figure 4. (a) HRTEM image of the interface between the TiO_2 core and $Li_4Ti_5O_{12}$ nanoshell of the LTO−TiO_2 nanofiber, and the respective FFT images taken on the region of the (b−d) core: (b) isolated TiO_2(B), (c) isolated anatase TiO_2, (d) overall, and (e) $Li_4Ti_5O_{12}$ nanoshell.

https://doi.org/10.1021/acsaem.3c01213
ACS Appl. Energy Mater. 2023, 6, 11433−11441

shell nanostructure. These jagged-shaped nanocrystals are composed of LTO, as indicated by the LTO(111) and (311) lattice fringes in HRTEM (Figure 3d) and the corresponding diffraction spots in the fast Fourier transform (FFT) image (Figure 3e). The core of the nanofiber remains as TiO_2, as identified by the TiO_2(B)(200) lattice fringes (Figure 3d) and diffraction spots (Figure 3f) of TiO_2. Further SAED analysis is performed to identify anatase TiO_2 and TiO_2(B) in the nanofiber of LTO−TiO_2. As shown in the SAED of the LTO−TiO_2 in Figure S2, clearly there is no overlap of the diffraction spots of TiO_2(B) and anatase TiO_2, corresponding to *d*-spacing of (200), (101) TiO_2(B) planes, and (101) anatase TiO_2 plane in agreement to HR-XRD results.

Additional HRTEM analysis is performed on the interface between the jagged-shaped LTO nanoshell and the nanofiber core. As observed in Figure 4a, there is a clear boundary between the $Li_4Ti_5O_{12}$ nanoshell and the TiO_2 core. From the lower region of Figure 4a, the LTO nanoshell on the TiO_2 core is composed purely of LTO with *d*-spacing of 0.16 and 0.26 nm, corresponding to the (333) and (311) lattice fringes, respectively, and their respective diffraction spots can be clearly observed in Figure 4e. Meanwhile, the nanofiber core (upper section of Figure 4a) consists of both TiO_2(B) and anatase TiO_2, as confirmed by their corresponding lattice fringes and diffraction spots (Figure 4d)—(110) and (200) for TiO_2(B), and (101) for anatase TiO_2. This overall FFT image of the TiO_2 core (Figure 4d) is further isolated into individual components as TiO_2(B) (Figure 4b), and anatase TiO_2 (Figure 4c). Again, anatase TiO_2 and TiO_2(B) show different specific patterns of diffraction spots that do not overlap. Thus, anatase TiO_2 and TiO_2(B) can be distinguished. Anatase TiO_2 is not detected in the nanoshell, but is present in the core of the nanofibers locally adjacent to TiO_2(B) particles. Such a zigzag pattern of TiO_2(B) and anatase TiO_2 is commonly observed in the TiO_2(B) nanofiber because of the perfect lattice matching between certain lattice planes of TiO_2(B) and anatase TiO_2.[22] As evident from Figure 4a, zigzag interfaces between the planes of $TiO_2(B)_{(110)}$ and anatase $TiO_{2(101)}$ are mainly observed in the TiO_2 core. By calculating the lattice mismatch of TiO_2(B)(110) and anatase TiO_2(101) between these two planes using the general definition given by $(d_{TB} - d_{TA})/d_{TB}$, [where *d* is the interplanar spacing (nm) of the corresponding plane], the lattice mismatch is small (mere 3.1% from Table 2a). This is in agreement with literature results.

The mechanism leading to the formation of a preferential LTO−TiO_2 core−shell morphology is proposed. During synthesis, the TiO_2 core are uniformly covered by an amorphous TiO_2 layer, as an intermediate step, prior to the formation of LTO−TiO_2 (Figure 1). The major (020), (200), and (001) lattice planes of the TiO_2 core observed in XRD are not exposed. Instead, the amorphous TiO_2 buffer layer prevents the preferential growth of LTO on the (020) lattice plane of TiO_2(B). LTO is converted via lithiation from the amorphous TiO_2 coating, leading to a core/shell TiO_2/$Li_4Ti_5O_{12}$ configuration, as demonstrated by the interface (i) between $Li_4Ti_5O_{12(311)}$ and anatase $TiO_{2(101)}$ planes and (ii) $Li_4Ti_5O_{12(333)}$ and $TiO_2(B)_{(110)}$ planes (observed in the HRTEM image in Figure 4a). The corresponding lattice mismatch between $Li_4Ti_5O_{12(311)}$ and anatase $TiO_{2(101)}$ is calculated to be 27.7% (Table 2b). This lattice mismatch is significantly lower than that of the anatase TiO_2(101) plane intersecting with other individual planes of $Li_4Ti_5O_{12}$ [i.e., (333), and (111)] as demonstrated in Table 2b and thus

Table 2. (a) Summary of Lattice Mismatches of TiO_2(B)/Anatase TiO_2 Interfaces in the Core of LTO−TiO_2 Nanofibers; (b) Summary of Lattice Mismatches of Anatase TiO_2/$Li_4Ti_5O_{12}$, and TiO_2(B)/$Li_4Ti_5O_{12}$ Interfaces of LTO−TiO_2[a]

(a)

Lattice mismatch w.r.t. TiO_2(B) (%)		TiO_2 anatase			
		(101) / *0.347*	(200) / *0.189*	(211) / *0.167*	(004) / *0.238*
TiO_2(B)	(110) / *0.358*	3.1	47.2	53.3	33.5
	(200) / *0.583*	40.5	67.6	71.4	51.5

(b)

Lattice mismatch w.r.t. TiO_2(B) (%)		$Li_4Ti_5O_{12}$	
		(333) / *0.16*	(311) / *0.251*
TiO_2 anatase	(101) / *0.347*	53.9	27.7
TiO_2(B)	(110) / *0.358*	55.3	29.9
TiO_2(B)	(200) / *0.583*	72.6	56.9

[a]*The interplanar spacing (unit in nm) is shown in italics underneath the corresponding lattice planes.* The green-shaded boxes are the major interfaces detected in LTO−TiO_2 using HRTEM analysis, while the green italic fonts represent planes observed in Figure 4a.

thermodynamically favors the nucleation and crystal growth of LTO from the (101) anatase TiO_2 lattice plane. As a result, the (311) plane of LTO tends to preferentially grow from the (101) anatase plane, while the interface between $Li_4Ti_5O_{12(333)}$ and $TiO_2(B)_{(110)}$ demonstrates preferential growth of the (333) plane of LTO from the (110) TiO_2(B) plane (as evident in Figure 4a). The LTO product is of high crystallinity with a well-defined morphology. The (111) plane of $Li_4Ti_5O_{12}$ is not observed at the interface between the TiO_2 core and $Li_4Ti_5O_{12}$ nanoshell, but rather at the outer diameter of the LTO nanoshell (as shown in Figure 3d). Since the (200) TiO_2(B) plane is perpendicular to the interface boundary, it is not a preferred direction to grow LTO, as evidenced from the larger lattice mismatch with $Li_4Ti_5O_{12}$, as shown in Table 2b.

The $Li_4Ti_5O_{12}$ nanoshell on the TiO_2 nanofiber (LTO−TiO_2) demonstrates superior performance as an anode for lithium-ion batteries, and its performance is summarized (Table 3) and compared to that of pristine TiO_2 (TiO_2) and bulk $Li_4Ti_5O_{12}$ (LTO). Bulk LTO is synthesized by conventional solid-state method. The cyclic voltammetry (CV) curve of LTO−TiO_2 (Figure 5a) shows a major reversible redox peak at 1.53/1.62 V versus Li^+/Li, corresponding to a combined peak of $Li_4Ti_5O_{12}$ and TiO_2(B). Another minor redox peak at 1.74/2.00 V versus Li^+/Li, corresponding to anatase TiO_2. The overall lithiation/delithiation process of LTO−TiO_2 nanofiber can be described as

$$\text{Anatase } TiO_2 + 0.5Li^+ + 0.5e^- \underset{\text{charge}}{\overset{\text{discharge}}{\rightleftharpoons}} Li_{0.5}TiO_2 \quad E_p{:}1.74\text{ V}/2.00\text{ V} \tag{1}$$

$$Li_4Ti_5O_{12} + TiO_2(B) + 4Li^+ + 4e^- \underset{\text{charge}}{\overset{\text{discharge}}{\rightleftharpoons}} Li_7Ti_5O_{12} + LiTiO_2 \quad E_p{:}1.53\text{ V}/1.63\text{ V} \tag{2}$$

https://doi.org/10.1021/acsaem.3c01213
ACS Appl. Energy Mater. 2023, 6, 11433−11441

Table 3. Summary of the Electrochemical Performance of LTO−TiO_2 and Pristine TiO_2

Samples	Discharge capacity ($mAhg^{-1}$)		First-cycle irreversible capacity loss		Discharge capacity retention after 1000 cycles	Energy density ($Wh\ kg^{-1}$)	SEI resistance (R_{SEI}) (Ω)	Charge transfer resistance (R_{CT}) (Ω)	Capacitance (C_d) (F)	Li-ion diffusion coefficient ($cm^2\ s^{-1}$)
	0.175 Ag^{-1}	1.75 Ag^{-1}	0.035 Ag^{-1}	1.75 Ag^{-1}	1.75 Ag^{-1}					
LTO-TiO_2	188	152	3 %	4 %	96 %	380	0	100 – 107	9.4×10^{-4}	2.6×10^{-8} – 2.8×10^{-8}
TiO_2	169	123	15 %	17%	75 %	263	98 – 120	103 – 128	7.1×10^{-3}	1.0×10^{-10} – 2.8×10^{-10}

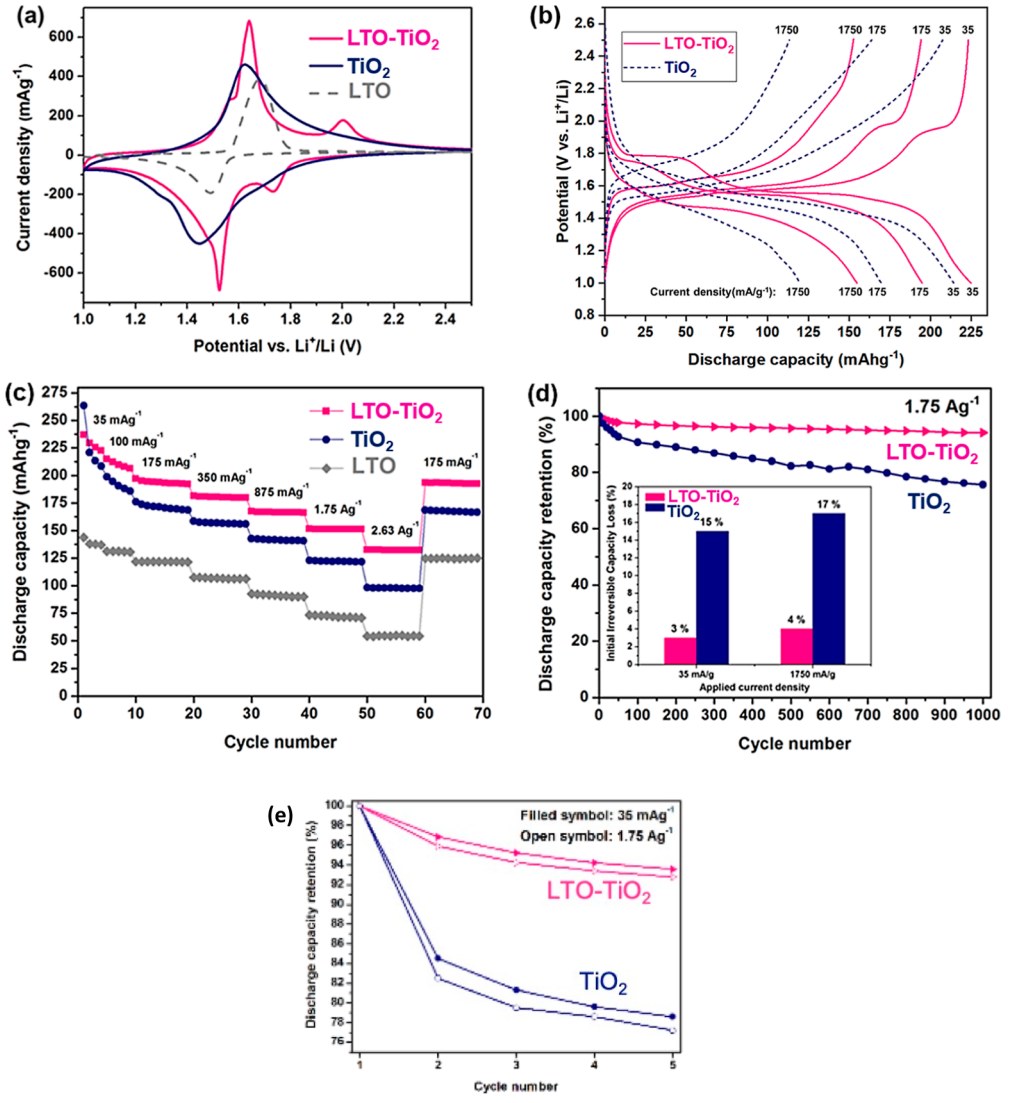

Figure 5. (a) CV curves of LTO−TiO_2, pristine TiO_2, and bulk LTO. (b) Discharge curves of LTO−TiO_2 and TiO_2 at different current densities from 35, 175, and 1750 mA g^{-1}. (c) Discharge rate capability performance of LTO−TiO_2, TiO_2, and bulk LTO, (d) long cycling performance of LTO−TiO_2 and TiO_2 in terms of discharge capacity retention, conducted at 1.75 A g^{-1} over 1000 cycles. Inset: initial irreversible discharge capacity loss (ICL) of LTO−TiO_2 and TiO_2 at 35 mA g^{-1} and 1.75 A g^{-1} at the first cycle. (e) Discharge capacity retention of LTO−TiO_2 and pristine TiO_2 nanofiber at a constant current charge/discharge of 35 mA g^{-1} (filled symbol) and 1.75 A g^{-1} (unfilled symbol) for the initial first five cycles.

As observed from the cyclic voltammograms in Figure 5a, LTO−TiO_2 has sharper redox peaks and higher peak current density than that of pristine TiO_2. This can be attributed to the reduced pesudocapacitive contribution from TiO_2(B) due to the $Li_4Ti_5O_{12}$ coverage on the TiO_2 core. As a result, the integrated peak area of LTO−TiO_2 is larger, suggesting a higher lithium storage capacity of LTO−TiO_2. The redox peak potential separation observed for the major peak (1.53/1.62 V) is 0.09 V for LTO−TiO_2, which is smaller than that of pristine TiO_2 (0.17 V) and bulk LTO (0.18 V) and hence lower polarization for LTO−TiO_2.

The discharge plateau for LTO−TiO_2 is flat and stable at all C-rates (Figure 5b). However, its capacity is not of equal contributions from anatase TiO_2, TiO_2(B), and $Li_4Ti_5O_{12}$ and

https://doi.org/10.1021/acsaem.3c01213
ACS Appl. Energy Mater. 2023, 6, 11433−11441

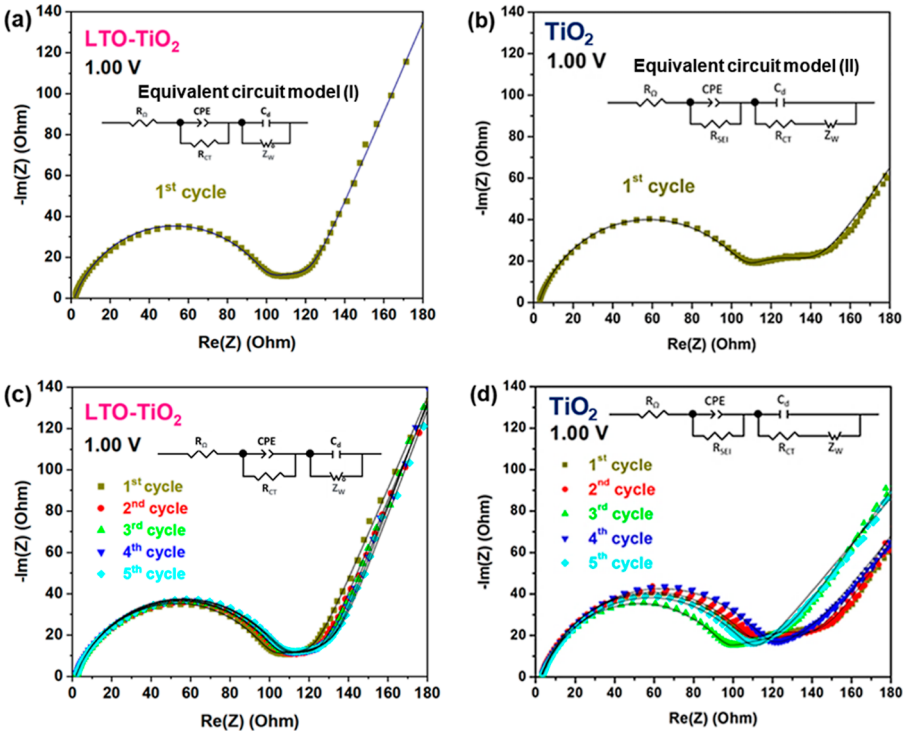

Figure 6. Nyquist plots (symbol) of (a,c) LTO−TiO_2 and (b,d) pristine TiO_2 at 1.00 V (i.e., at the end of each discharge cycle), over the initial five discharge/charge cycles, fitted by the respective equivalent circuit model shown in inset (solid line) with minimal fitting error.

highly dependent on the current applied. Capacity contribution from anatase TiO_2 is only apparent at low current density (low C-rate), whereas the combined effect of TiO_2(B) and $Li_4Ti_5O_{12}$ accounts for the major capacity contribution and stable discharge plateau at ∼1.5−1.55 V.

At low C-rates (35 and 175 mA g^{-1}), two discharge plateaus corresponding to anatase TiO_2 (1.74 V), and the combined effect of TiO_2(B) and LTO (1.53 V) can be observed in Figure 5b. The reverse charging plateau occurs at 1.63 V for the combined effect of TiO_2(B) and LTO, and at 2 V for anatase TiO_2, respectively. With increased current density, one discharge/charge voltage plateau is observed at 1.53 V/1.63 V corresponding to the combined effect of TiO_2(B) and LTO. As demonstrated by the disappearance of voltage plateau (1.74 V/2 V) corresponding to anatase TiO_2 in both charge and discharge curves of LTO−TiO_2 at high rate of 10 C (1.75 A g^{-1}) (Figure 5b), the lithiation and delithiation of anatase TiO_2 do not contribute to the capacity of the composite at high rate. Since anatase TiO_2 lithiates/delithiates through Faradic diffusion-controlled intercalation mechanism instead of the pseudocapacitive mechanism as observed for TiO_2(B); most of the capacity for LTO−TiO_2 is contributed from TiO_2(B) rather than anatase TiO_2, particularly at high C rates, despite the presence of anatase TiO_2 in LTO−TiO_2.

LTO−TiO_2 shows a superior rate capability and reversibility than pristine TiO_2 and bulk LTO. As shown in Figure 5c, at low applied current density of 35 and 100 mA g^{-1}, LTO−TiO_2 has a reversible discharge capacity of 226 and 210 mA h g^{-1}, respectively, a 6 and 10% higher than pristine TiO_2. When subjected to high-rate discharge at 1.75 and 2.63 A g^{-1}, the discharge capacity of LTO−TiO_2 can reach 152 and 133 mA h g^{-1}, respectively, which leads to a significant improvement of 24 and 35% compared to pristine TiO_2 at the same discharge rates. LTO−TiO_2 clearly demonstrates superior high-rate capability and reversibility. It should be noted that at the first cycle, the capacity of LTO−TiO_2 is lower than that of TiO_2, due to the lower theoretical capacity of LTO. There is a significant irreversible capacity loss observed in the first cycle of TiO_2 at 35 mA g^{-1} (from 263 to 223 mA h g^{-1}, i.e., 15% drop).

The initial irreversible capacity loss (ICL) of pristine TiO_2 can be effectively mitigated in LTO−TiO_2, so the discharge capacity of LTO−TiO_2 is consistently high. As shown in Figure 5d and inset, at 1.75 A g^{-1}, LTO−TiO_2 maintains a discharge capacity retention of 96% over 1000 cycles, equivalent to a mere 4% initial ICL (cf. 17% for TiO_2). At 35 mA g^{-1}, the initial ICL is slightly smaller at 3% (cf. 15% for TiO_2), and the discharge capacity retention of LTO−TiO_2 over 1000 cycles is 97%. This indicates that the uniform LTO coating on TiO_2 is effective in reducing the ICL to a negligible level. The initial irreversible capacity loss for the first five cycles is further studied for both LTO−TiO_2 and the pristine TiO_2 nanofiber (Figure 5e). When charge/discharge at a constant current of 35 mA g^{-1} and 1.75 A g^{-1}, LTO−TiO_2 shows the respective discharge capacity retention is 97 and 96% (Figure 5e), corresponding to the first cycle irreversible capacity loss of 3 and 4%. After five cycles, the capacity retention of LTO−TiO_2 is around 93% for both currents, corresponding to an initial irreversible capacity loss of 7%. Compared to the pristine TiO_2 nanofiber (TiO_2), the respective discharge capacity retention is 84 and 83% (Figure 5e) under constant charge/discharge currents of 35 mA g^{-1} and 1.75 A g^{-1}, corresponding to the first cycle irreversible capacity loss of 16 and 17%. After five cycles, the capacity retention of TiO_2 nanofiber is around 79 and 77% under constant charge/discharge currents of 35 mA g^{-1} and 1.75 A g^{-1}, corresponding to an initial irreversible capacity loss of 21 and 23%, respectively. Clearly, the first cycle irreversible capacity loss of LTO−TiO_2 is significantly reduced

https://doi.org/10.1021/acsaem.3c01213
ACS Appl. Energy Mater. 2023, 6, 11433−11441

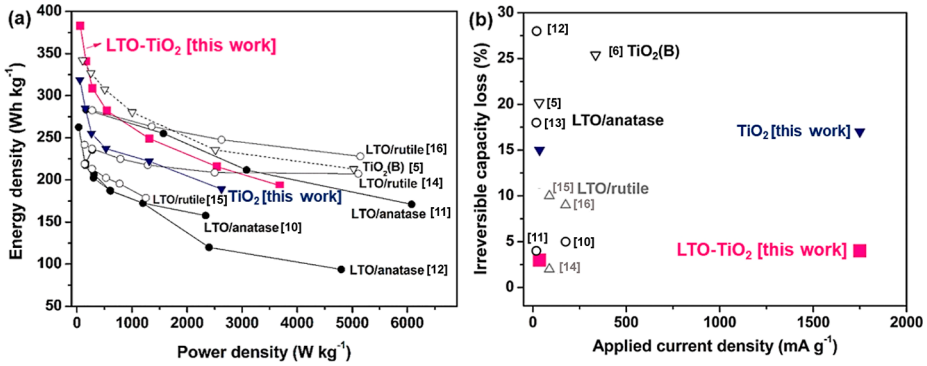

Figure 7. (a) Ragone plot and (b) initial irreversible capacity loss of LTO−TiO_2 (pink ■) and pristine TiO_2 (blue ▼), compared to those $Li_4Ti_5O_{12}/TiO_2$ composites and TiO_2(B) reported in literature. Among the irreversible capacity loss reported in literature, only low discharge current performance (17.5−250 mA g^{-1}) is reported for TiO_2-based materials.

to 4% at a high current density of 1.75 A g^{-1} due to the introduction of LTO coating which prevented SEI formation of TiO_2. This aligns with the results from the EIS study in the latter section.

The $Li_4Ti_5O_{12}$−TiO_2 core−shell structure can lead to negligible SEI formation and enhanced charge transfer, as evident from the electrochemical impedance spectroscopy (EIS) for the initial five charge/discharge cycles. As shown in Figure 6a,c, only one depressed semicircle is observed in the Nyquist plots of LTO−TiO_2 at the end of each discharge cycle over five cycles, and these impedance data can be well-fitted by equivalent circuit model (I) (shown as inset of Figure 6a,c) with Ohmic resistance (R_{ohm}), charge transfer resistance (R_{CT}) and capacitor component (C_d) contributed from TiO_2, but no SEI impedance (R_{SEI}) component, under minimum and negligible fitting error. Hence, the R_{SEI} for LTO−TiO_2 maintains 0 Ω over the initial five cycles (Table S1), aligns with the negligible decrease in initial capacity observed in experimental charge/discharge (inset of Figure 5d). In contrast, the Nyquist plots of TiO_2 (Figure 6b,d) show two depressed semi circles, which can only be fitted by equivalent circuit model (II) (shown as inset of Figure 6b,d) with additional component ascribed to SEI. The additional semicircle observed is ascribed to the SEI formed on the electrode. The R_{SEI} for TiO_2 is 110 Ω at the end of the first cycle discharge (derived from Figure 6b), which is significantly higher than that of LTO−TiO_2 (0 Ω). Over five cycles, R_{SEI} of TiO_2 is unstable with large fluctuations (Figure 6d) (108.4 Ω ± 10.1%); such unstable SEI on TiO_2 can be readily removed, resulting in immediate re-exposure of TiO_2 surfaces to the electrolyte for new SEI formation aggregated upon subsequent discharge, thereby larger initial capacity loss accumulated.

To further demonstrate that LTO−TiO_2 does not show any SEI resistance, we fit the Nyquist plot of LTO−TiO_2 using the equivalent circuit model (II) of TiO_2 which has an SEI component. As shown in Figure S3, the fitted line, with SEI component (red curve) does not match the corresponding impedance data of LTO−TiO_2, with an error of 26.7%, showing an additional semicircle (R_{SEI} = 31.5 Ω) and the low frequency slope cannot be modeled properly. In contrast, this equivalent circuit model (II) can perfectly fit the Nyquist plot of TiO_2 with a minimum error (0.07%) (Figure 6b). We also perform extra EIS study on bare LTO. No SEI component is observed for the Nyquist plot of bare LTO and LTO−TiO_2, suggesting the LTO nanoshell does prevent the growth of SEI from TiO_2. As shown in Figure S4, the Nyquist plot of bare LTO shows one semicircle, which can only be well-fitted by equivalent circuit model without capacitor (c_d) and SEI impedance (R_{SEI}) components (fitting error: 0.04%).

In addition, over cycling, as demonstrated in Tables S1 and S2, LTO−TiO_2 has lower charge transfer resistance (R_{CT}) (110 Ω), and more than 250 times higher lithium-ion diffusion coefficient (D_{Li}) (2.56−2.81 × 10^{-8} cm^2 s^{-1}) than pristine TiO_2 (1.04 × 10^{-10} cm^2 s^{-1}) shown in Tables S1 and S3. This demonstrates that the LTO coverage can eliminate the SEI formation of TiO_2, including TiO_2(B) to a negligible level, leading to a significant reduction in ICL, thereby enhanced capacity and high-rate cyclability. Also, the presence of $Li_4Ti_5O_{12}/TiO_2$ interfaces in LTO−TiO_2 can serve as low-energy barriers for charge transport and hence reduces R_{CT}. The presence of the SEI layer on TiO_2 hinders the lithium-ion transport, resulting in large R_{CT} and small D_{Li}.

The electrochemical performance of LTO−TiO_2 nanofibers and pristine TiO_2 are summarized in Table 3, and their energy density, power density, and initial irreversible capacity loss are compared to the LTO−TiO_2 composites and TiO_2(B) reported in the literature[5,6,10−16] (Figure 7). As shown in the Ragone plot in Figure 7a, LTO−TiO_2 shows the highest energy density (250−400 W h kg^{-1}) within the power density range sufficient for grid energy storage (<1000 kW g^{-1}). LTO−TiO_2 in this work can achieve the lowest initial irreversible capacity loss even at a high current density of 1.75 A g^{-1} or as low as 35 mA g^{-1}, as shown in Figure 7b. Among the irreversible capacity loss reported in literature, only low discharge current performance below 250 mA g^{-1} are reported for TiO_2-based materials. This suggests that LTO−TiO_2 can cater to the need of high-performance electrode materials for energy storage. In principle, the electrochemical performance of LTO−TiO_2 can be further optimized by varying the composition ratio between $Li_4Ti_5O_{12}$ and TiO_2, and the thickness of the LTO nanoshell, depending on application.

■ CONCLUSIONS

We have developed a synthesis strategy to achieve uniform $Li_4Ti_5O_{12}$ (LTO) coverage on TiO_2 nanofibers (LTO−TiO_2) consisting of a mixed phase of anatase TiO_2 and TiO_2(B). LTO is formed by the lithiation of the amorphous TiO_2 bridge layer on pristine TiO_2 fibers. The bridge layer promotes growth of the preferential LTO plane from the respective TiO_2 planes. When applied as an anode material for Li-ion batteries, LTO−TiO_2 exhibits stable high rate capability and cyclability

https://doi.org/10.1021/acsaem.3c01213
ACS Appl. Energy Mater. 2023, 6, 11433−11441

with negligible initial irreversible capacity loss compared to pristine TiO_2. The uniform LTO coverage can effectively protect TiO_2 from SEI formation, leading to negligible SEI resistance. The presence of abundant $Li_4Ti_5O_{12}/TiO_2$ nanointerfaces can facilitate charge transfer. Both factors contribute to the enhanced electrochemical performance and stability, leading to a high energy density of LTO−TiO_2 nanofibers. This work demonstrates that our $Li_4Ti_5O_{12}$ nanoshell on TiO_2 nanofibers can be utilized as a viable energy storage material with superior performance and high energy density. It also gives insights into the strategy of using $Li_4Ti_5O_{12}$ coating to eliminate the initial irreversible capacity loss of other electrode materials.

■ ASSOCIATED CONTENT

Supporting Information

The Supporting Information is available free of charge at https://pubs.acs.org/doi/10.1021/acsaem.3c01213.

TEM images and HRTEM image of pristine TiO_2 nanofiber with the respective FFT image; SAED pattern of the LTO−TiO_2 nanofiber; additional Nyquist plots of LTO−TiO_2 and LTO at 1.00 V, fitted by different equivalent circuit models; summary of the charge transfer resistance and lithium-ion diffusion coefficient of LTO−TiO_2 and TiO_2; and summary of the EIS results of LTO−TiO_2 and TiO_2 for the initial five discharge/charge cycles (PDF)

■ AUTHOR INFORMATION

Corresponding Authors

Chi-Ying Vanessa Li − *Department of Chemistry, University of Hong Kong, Pokfulam, Hong Kong; Hong Kong Quantum AI Lab Limited (HKQAI), Sha-Tin, Hong Kong;* orcid.org/0000-0003-2559-9550; Email: cyvli@hku.hk

Kwong-Yu Chan − *Department of Chemistry, University of Hong Kong, Pokfulam, Hong Kong;* orcid.org/0000-0002-4124-2562; Email: hrsccky@hku.hk

Authors

Ching-Kit Ho − *Department of Chemistry, University of Hong Kong, Pokfulam, Hong Kong; Hong Kong Quantum AI Lab Limited (HKQAI), Sha-Tin, Hong Kong*

Changzhong Liao − *Department of Chemistry, University of Hong Kong, Pokfulam, Hong Kong*

Yee-Yan Tay − *School of Materials Science and Engineering, Facility for Analysis, Characterization, Testing and Simulation (FACTS), Nanyang Technological University, Singapore 639798, Singapore*

Ka-Ming Leung − *Department of Chemistry, University of Hong Kong, Pokfulam, Hong Kong; Hong Kong Quantum AI Lab Limited (HKQAI), Sha-Tin, Hong Kong*

Chi-Kin Jenkin Tsui − *Department of Chemistry, University of Hong Kong, Pokfulam, Hong Kong; Hong Kong Quantum AI Lab Limited (HKQAI), Sha-Tin, Hong Kong*

GuanHua Chen − *Department of Chemistry, University of Hong Kong, Pokfulam, Hong Kong; Hong Kong Quantum AI Lab Limited (HKQAI), Sha-Tin, Hong Kong*

Complete contact information is available at: https://pubs.acs.org/10.1021/acsaem.3c01213

Author Contributions

‖C.L., Y.-Y.T., and K.-M.L. contributed equally.

Notes

The authors declare no competing financial interest.

■ ACKNOWLEDGMENTS

This work was financially supported by AIR@InnoHK Clusters and ITF Research Talent Hub (PiH/850/21, PiH/851/21, and InP/805/21) by the Innovation and Technology Commission of the HKSAR Government and Theme-based research grant from Research Grant Commission of the HKSAR (project no. T23-601/17-R). The authors would like to acknowledge the use of HR-XRD (operated by Dr. Shengshou Ma) in the laboratory of Prof. Kaimin Shih of Civil Engineering in The University of Hong Kong (HKU) and the use of electron microscopy in Electron Microscope Unit, HKU. We would also like to acknowledge the Facility for Analysis, Characterization, Testing and Simulation (FACTS), Nanyang Technological University, Singapore, for use of their electron microscopy (HR-TEM).

■ REFERENCES

(1) Chen, Z.; Belharouak, I.; Sun, Y. K.; Amine, K. Titanium-Based Anode Materials for Safe Lithium-Ion Batteries. *Adv. Funct. Mater.* **2013**, *23* (8), 959−969.

(2) Brutti, S.; Gentili, V.; Menard, H.; Scrosati, B.; Bruce, P. G. TiO_2-(B) Nanotubes as Anodes for Lithium Batteries: Origin and Mitigation of Irreversible Capacity. *Adv. Energy Mater.* **2012**, *2*, 322−327.

(3) Dylla, A. G.; Lee, J. A.; Stevenson, K. J. Influence of Mesoporosity on Lithium-Ion Storage Capacity and Rate Performance of Nanostructured TiO_2(B). *Langmuir* **2012**, *28*, 2897−2903.

(4) Tang, Y.; Zhang, Y.; Deng, J.; Wei, J.; Tam, H. L.; Chandran, B. K.; Dong, Z.; Chen, Z.; Chen, X. Mechanical Force-driven Growth of Elongated Bending TiO_2-based Nanotubular Materials for Ultrafast Rechargeable Lithium Ion Batteries. *Adv. Mater.* **2014**, *26* (35), 6111−6118.

(5) Zhang, W.; Cai, L.; Cao, S.; Qiao, L.; Zeng, Y.; Zhu, Z.; Lv, Z.; Xia, H.; Zhong, L.; Zhang, H.; Ge, X.; Wei, J.; Xi, S.; Du, Y.; Li, S.; Chen, X. Interfacial Lattice-Strain-Driven Generation of Oxygen Vacancies in an Aerobic-annealed TiO_2(B) Electrode. *Adv. Mater.* **2019**, *31* (52), 1906156.

(6) Wang, S.; Qu, D.; Jiang, Y.; Xiong, W. S.; Sang, H. Q.; He, R. X.; Tai, Q.; Chen, B.; Liu, Y.; Zhao, X. Z. Three-Dimensional Branched TiO_2 Architectures in Controllable Bloom for Advanced Lithium-ion Batteries. *ACS Appl. Mater. Interfaces* **2016**, *8* (31), 20040−20047.

(7) Yan, X.; Li, Y.; Li, M.; Jin, Y.; Du, F.; Chen, G.; Wei, Y. Ultrafast Lithium Storage in TiO_2-bronze Nanowires/N-doped Graphene Nanocomposites. *J. Mater. Chem. A* **2015**, *3* (8), 4180−4187.

(8) Ohzuku, T.; Ueda, A.; Yamamoto, N. Zero-Strain Insertion Material of $Li[Li_{1/3}Ti_{5/3}]O_4$ for Rechargeable Lithium Cells. *J. Electrochem. Soc.* **1995**, *142* (5), 1431−1435.

(9) Rahman, M. M.; Wang, J.-Z.; Hassan, M. F.; Wexler, D.; Liu, H. K.; Amorphous Carbon Coated High Grain Boundary Density Dual Phase $Li_4Ti_5O_{12}$-TiO_2: A Nanocomposite Anode Material for Li-Ion Batteries. *Adv. Energy Mater.* **2011**, *1* (2), 212−220.

(10) Liao, J.-Y.; Chabot, V.; Gu, M.; Wang, C.; Xiao, X.; Chen, Z. Dual Phase $Li_4Ti_5O_{12}$-TiO_2 Nanowire Arrays as Integrated Anodes for High-rate Lithium-ion Batteries. *Nano Energy* **2014**, *9*, 383−391.

(11) Stenina, I. A.; Kulova, T. L.; Skundin, A. M.; Yaroslavtsev, A. B. High Grain Boundary Density $Li_4Ti_5O_{12}$/Anatase-TiO_2 Nanocomposites as Anode Material for Li-ion Batteries. *Mater. Res. Bull.* **2016**, *75*, 178−184.

(12) Jiang, Y.-M.; Wang, K.-X.; Wu, X.-Y.; Zhang, H.-J.; Bartlett, B. M.; Chen, J.-S. $Li_4Ti_5O_{12}/TiO_2$ Hollow Spheres Composed Nanoflakes with Preferentially Exposed $Li_4Ti_5O_{12}$ (011) Facets for High-Rate Lithium Ion Batteries. *ACS Appl. Mater. Interfaces* **2014**, *6* (22), 19791−19796.

(13) Zhao, X.; Liu, H.; Feng, Y.; Pang, L.; Ding, M.; Deng, L.; Zhu, J. In-situ Constructing of Hierarchical $Li_4Ti_5O_{12}$-TiO_2 Microspheres Assembled by Nanosheets for Lithium-Ion Batteries. *Mater. Lett.* **2018**, *231*, 130−133.
(14) Li, X.-P.; Mao, J. A $Li_4Ti_5O_{12}$-rutile TiO_2 Nanocomposite with an Excellent High Rate Cycling Stability for Lithium Ion Batteries. *New J. Chem.* **2015**, *39* (6), 4430−4436.
(15) Yi, T.-F.; Fang, Z.-K.; Xie, Y.; Zhu, Y.-R.; Yang, S.-Y. Rapid Charge-Discharge Property of $Li_4Ti_5O_{12}$-TiO_2 Nanosheet and Nanotube Composites as Anode Material for Power Lithium-Ion Batteries. *ACS Appl. Mater. Interfaces* **2014**, *6* (22), 20205−20213.
(16) Wu, L.; Leng, X.; Liu, Y.; Wei, S.; Li, C.; Wang, G.; Lian, J.; Jiang, Q.; Nie, A.; Zhang, T.-Y. A Strategy for Synthesis of Nanosheets Consisting of Alternating Spinel $Li_4Ti_5O_{12}$ and Rutile TiO_2 Lamellas for High-Rate Anodes of Lithium-Ion Batteries. *ACS Appl. Mater. Interfaces* **2017**, *9* (5), 4649−4657.
(17) Wu, Q.; Xu, J.; Yang, X.; Lu, F.; He, S.; Yang, J.; Fan, H. J.; Wu, M. Ultrathin Anatase TiO_2 Nanosheets Embedded with TiO_2-B Nanodomains for Lithium-Ion Storage: Capacity Enhancement by Phase Boundaries. *Adv. Energy Mater.* **2015**, *5* (7), 1401756.
(18) Cui, P.; Xie, B.; Li, X.; Li, M.; Li, Y.; Wang, Y.; Liu, Z.; Liu, X.; Huang, J.; Song, D.; Mbengue, J. M. Anatase/TiO_2-B Hybrid Microspheres Constructed from Ultrathin Nanosheets: Facile Synthesis and Application for Fast Lithium Ion Storage. *CrystEngComm* **2015**, *17* (41), 7930−7937.
(19) Tian, Q.; Zhang, Z.; Yang, L.; Hirano, S.-i. Morphology-engineered and TiO_2(B)-Introduced Anatase TiO_2 as an Advanced Anode Material for Lithium-Ion Batteries. *J. Mater. Chem. A* **2015**, *3* (28), 14721−14730.
(20) Wang, Y.-Q.; Gu, L.; Guo, Y.-G.; Li, H.; He, X.-Q.; Tsukimoto, S.; Ikuhara, Y.; Wan, L.-J. Rutile-TiO_2 Nanocoating for a High-Rate $Li_4Ti_5O_{12}$ Anode of a Lithium-Ion Battery. *J. Am. Chem. Soc.* **2012**, *134* (18), 7874−7879.
(21) Ho, C.-K.; Li, C.-Y. V.; Chan, K.-Y.; Yung, H.; Tay, Y.-Y. Interfacing TiO_2(B) Nanofibers with $Li_4Ti_5O_{12}$ Towards Highly Reversible and Durable TiO_2-based Anode for Li-Ion Batteries. *Energy Technol.* **2019**, *7*, 107−112.
(22) Li, W.; Liu, C.; Zhou, Y.; Bai, Y.; Feng, X.; Yang, Z.; Lu, L.; Lu, X.; Chan, K. Y. Enhanced Photocatalytic Activity in Anatase/TiO_2 (B) Core-Shell Nanofiber. *J. Phys. Chem. C* **2008**, *112* (51), 20539−20545.

https://doi.org/10.1021/acsaem.3c01213
ACS Appl. Energy Mater. 2023, 6, 11433−11441